Eddy-Induced Heat Transport in the Subtropical North Pacific from Argo, TMI, and Altimetry Measurements

BO QIU AND SHUIMING CHEN

Department of Oceanography, University of Hawaii at Manoa, Honolulu, Hawaii

ABSTRACT

Basin-scale heat transport induced by mesoscale oceanic eddies is estimated by combining satellite-derived sea surface height and temperature [temperature data are from the TRMM Microwave Imager (TMI)] data with Argo float temperature–salinity data. In the North Pacific Ocean subtropical gyre, warm (cold) temperature anomalies of mesoscale eddies are found to be consistently located to the west of high (low) SSH anomalies. The phase misalignment between the temperature and velocity anomalies, however, is largely confined to the seasonal thermocline, causing most of the eddy-induced heat transport to be carried in the surface 200-m layer. By establishing a statistical relationship between the surface and depth-integrated values of the eddy heat transport, the basin-scale eddy heat transport is derived from the concurrent satellite SSH/SST data of the past six years. In the Kuroshio Extension region, the meandering zonal jet is found to generate oppositely signed eddy heat fluxes. As a result, the zonally integrated poleward heat transport associated with the Kuroshio Extension is at a level $O(0.1$ PW), smaller than the previous estimates based on turbulent closure schemes. Large poleward eddy heat transport is also found in the subtropical North Pacific along a southwest–northeast-tilting band between Taiwan and the Midway Islands. This band corresponds to the region of the subtropical front, and it is argued that the relevant temperature field for identifying this band in the turbulent closure scheme models should be that averaged over the seasonal thermocline.

1. Introduction

Over the past two decades, many studies have investigated the ocean's role in closing the global heat balance, and a consensus has emerged that the time-mean ocean circulation carries about one-third to one-half of the excess heat from the Tropics to the Poles. A rich literature now exists that addresses the north–south ocean heat transport and comprehensive recent reviews can be found in Trenberth and Caron (2001), Bryden and Imawaki (2001), Jayne and Marotzke (2001), and Talley (2003). With the ocean being a turbulent medium in which the time-mean circulation is in general much weaker than its time-varying signals, several recent studies have started to look into the heat transport carried by mesoscale eddies of the ocean.

By analyzing historical moored in situ current meter and temperature records, Wunsch (1999) noted that eddy-induced heat fluxes are important relative to the total meridional heat fluxes in western boundary current (WBC) regions of the North Atlantic and Pacific Oceans. While the paucity of the mooring coverage prevented him from a quantitative estimation, Wunsch suggested that eddy flux convergences could potentially affect heat balances of the ocean in regions outside of the WBCs as well.

The importance of the eddy heat transport near the tropical/subtropical gyre boundary of the North Pacific Ocean was recently emphasized by Roemmich and Gilson (2001). Based on high-resolution XBT/XCTD data from repeat transects connecting San Francisco, Honolulu, Guam, and Taiwan, Roemmich and Gilson showed that the basinwide eddy-induced poleward heat transport averages 0.086 ± 0.012 PW. While this transport represents only 15% of the total mean northward oceanic heat transport across this section (Roemmich et al. 2001), they found that the mesoscale eddies are a major contributor to the observed *time-varying* meridional heat transport. From a composite analysis, Roemmich and Gilson (2001) further showed that centers of both the observed warm- and cold-core eddies tilt westward with decreasing depth. With the vertical shear of the mean zonal flow in the region being positive, this observed vertical eddy structure is consistent with Qiu's (1999) conclusion that baroclinic instability is the mechanism for the enhanced eddy activity in the latitudinal band between Hawaii and Taiwan.

Given the difficulties in measuring mesoscale eddies on a global basis, efforts have also been made in the

Corresponding author address: Dr. Bo Qiu, Department of Oceanography, University of Hawaii at Manoa, 1000 Pope Road, Honolulu, HI 96822.
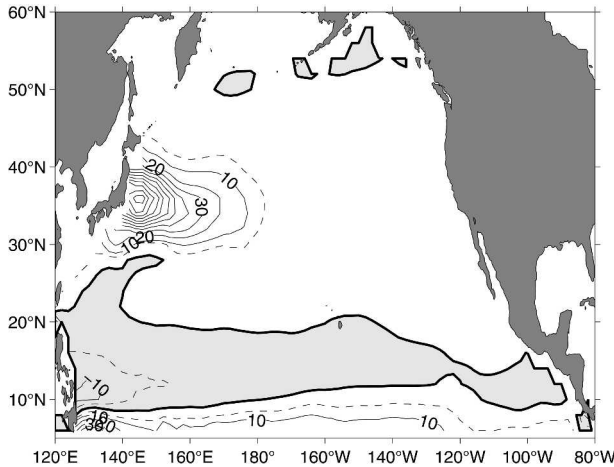E-mail: bo@soest.hawaii.edu

FIG. 1. Meridional eddy heat flux inferred from $-\rho c_p \kappa \partial \overline{T}/\partial y$. Here, the eddy diffusivity κ is estimated by SUW based on 9 yr of T/P SSH data, and $\partial \overline{T}/\partial y$ is calculated from the *WOA01* (Conkright et al. 2002) annual mean temperature climatology averaged in the upper 1000-m layer. Contour intervals are 10×10^6 W m^{-1} for solid lines and 5×10^6 W m^{-1} for dashed lines. The maximum eddy heat flux value in the Kuroshio Extension region east of Japan is $\sim110 \times 10^6$ W m^{-1}. Shaded areas indicate equatorward eddy heat transport.

past to use turbulent closure schemes to relate satellite altimeter-derived eddy activity to the meridional eddy heat fluxes. Assuming the conditions of statistically homogeneous, barotropic, β-plane turbulence, Holloway (1986) and Keffer and Holloway (1988) proposed that the eddy diffusivity for a passive tracer be given by $\kappa \simeq C\tau\psi$, where C is a proportionality constant (~0.4), τ is an $O(1)$ anisotropy tensor accounting for Rossby wave propagation, and ψ is the rms geostrophic streamfunction. By relating ψ to the rms sea surface height (SSH) signals of *Seasat* and by using the mean temperature $\overline{T}$ data from Levitus climatology, they estimated the eddy heat transport as a form of Fickian diffusion: $\mathbf{v}'T' = -\kappa\nabla_h\overline{T}$.

By adopting a "mixing length" hypothesis, Stammer (1998) proposed an alternative formula for estimating the eddy diffusivity: $\kappa = 2\alpha K_E T_{\text{alt}}$. Here α is a scaling factor (~0.005) accounting for both the efficiency of individual eddies to mix tracer particles and the conversion from the altimetric surface eddy kinetic energy (EKE) values, K_E, to an average EKE over the top 1000 m of the thermocline; T_{alt} is the integral time scale estimated from autocovariance of the altimetric SSH data. Using the Ocean Topography Experiment (TOPEX)/Poseidon (T/P) SSH data and Levitus and Boyer (1994) temperature climatology, Stammer (1998) estimated the meridional eddy heat transport for the global ocean. This 1998 study was recently updated by Stammer et al. (2003, manuscript submitted to *J. Phys. Oceanogr.*, hereinafter SUW) with the use of a longer time series of the T/P SSH data, and the meridional eddy heat transport in the North Pacific based on their

updated κ value is presented in Fig. 1. Strong poleward eddy heat transports in the North Pacific occur in the Kuroshio Extension region and along the equatorial band. In the interior eastern Pacific, the eddy heat transport is generally small. In the subtropical North Pacific, a zero transport line runs parallel to $\sim20°$N, and the eddy heat transport is dominantly *equatorward* in the band of $10°-20°$N. Use of Holloway's (1986) formula for κ leads to a geographical distribution for the meridional eddy heat transport similar to that shown in Fig. 1.

The approaches of Holloway (1986) and Stammer (1998) assumed that eddy-induced heat fluxes are always downgradient and several ad hoc scaling factors have been included in their formulations for κ. Using a high-resolution ocean general circulation model (OGCM), Jayne and Marotzke (2002) estimated recently the eddy heat transport directly from the model output and compared it with the estimate by Stammer (1998). While finding a qualitative agreement between the two estimates, they also pointed out two noticeable differences. In the WBC regions, Jayne and Marotzke showed that while a meandering jet can have high levels of EKE (and hence, a large apparent eddy diffusivity), it may not necessarily have the associated high level of eddy heat transport. In the equatorial Pacific Ocean, they presented evidence that there are regions where the eddy heat transport is upgradient, rather than downgradient as assumed for Fickian diffusion.

With new observational ability to measure mesoscale eddy activity becoming available in recent years, we attempt in this study to reevaluate the eddy heat transport in the North Pacific. In contrast to the studies by Holloway (1986) and Stammer (1998) in which satellite altimetry data were used to derive the statistical properties of the mesoscale eddy field, the satellite SSH data will be used in this study to evaluate the movement and strength of individual mesoscale eddies. In addition to the satellite altimetry data, we will also in this study utilize the sea surface temperature (SST) data measured by the Tropical Rainfall Measuring Mission (TRMM) Microwave Imager and the in situ temperature and salinity data from the global Argo float program. These two datasets have become available recently and, as we will show below, provide us with an effective means to capture the thermal structures of the mesoscale eddies. By combining the concurrent temperature and surface dynamic height measurements, we seek to estimate the eddy heat flux $v'T'$ directly.

Section 2 provides a brief description of the satellite altimetric, the TRMM Microwave Imager, and the Argo profiling float data. In section 3, we show examples on how these three datasets can be synthesized to capture the temperature and velocity structures of mesoscale eddies. Differences are found between the vertical heat transport structures of the tropical and subtropical mesoscale eddies. In section 4, a method is proposed for calculating the large-scale eddy heat
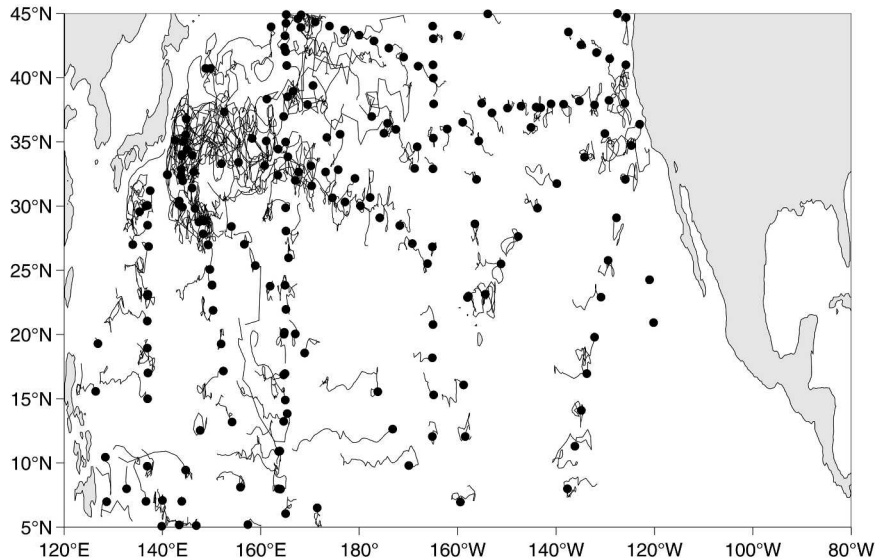
FIG. 2. Trajectories of the 217 Argo floats with profiling depths ≥1500 m in the North Pacific during Apr 1999–Jan 2004. Dark circles indicate the locations of deployment.

fluxes in the subtropical basin of the North Pacific. The results are interpreted in light of the regional ocean circulation and are compared with those estimated by the previous studies. A summary of the study is given in section 5.

2. Data

a. In situ Argo float data

The global Argo float project was initiated in 1998 to collect temperature–salinity ($T–S$) profiles of the world oceans on a broad spatial scale (Argo Science Team 2001). The profiling floats conduct $T–S$ measurements nominally every 10 days as they rise from the targeted parking depth of 2000 dbar. Figure 2 shows the available Argo floats and their trajectories in the North Pacific Ocean. The 217 floats shown in Fig. 2 all have their profiling depths ≥1500 m and they span the period from April 1999 to January 2004. For each profile, a delayed-mode quality control is conducted following the procedure proposed by Wong et al. (2003). It compares the measured $\theta–S$ data against the regional $\theta–S$ climatology and removes anomalous profiles affected by salinity sensor drift. The number of valid $T–S$ profiles used in this study totals 8826.

b. TMI SST data

By measuring SSTs using microwave radiometry, the TRMM Microwave Imager (TMI) can see through clouds with little attenuation (Wentz et al. 2000). The usefulness of the TMI data in capturing mesoscale SST features has been demonstrated by several recent studies (e.g., Chelton et al. 2001; Nonaka and Xie 2003). For this study, we use the weekly mean SST product on a 0.25° × 0.25° grid. The product covers the period from

December 1997 to October 2003. Because the TMI measurements extend only as far north as 38°N, this latitude marks the northern boundary for our analysis based on the TMI dataset.

c. Satellite altimetric data

Satellite altimetry data are used in this study to capture the surface dynamic signals of individual mesoscale eddies. For this purpose, we use the global SSH anomaly dataset compiled by the CLS Space Oceanographic Division of Toulouse, France. The dataset merges the T/P and *European Remote Sensing Satellites 1* and *2* (*ERS-1/2*) along-track SSH measurements and has a much improved capability of detecting the mesoscale SSH signals (Le Traon and Dibarboure 1999; Ducet et al. 2000). The CLS SSH dataset used in this study has a 7-day temporal resolution, a ⅓° × ⅓° spatial resolution, and covers the period from October 1992 to October 2003.

3. Structures of mesoscale eddies

Before discussing the eddy heat transport on a basin scale, it is useful to examine first the vertical temperature structures of individual mesoscale eddies. As noted by Bennett and White (1986) and Roemmich and Gilson (2001), a geostrophic eddy would contribute to no *net* heat transport, unless a vertical phase tilt exists in the temperature profile associated with the eddy. Because of their different vertical structures of eddy-induced heat transport, we will discuss the tropical and subtropical regions separately below.

a. The subtropical gyre

We will focus in this subsection on an Argo float (WMO ID: 29033) that was deployed at 30.1°N, 142.5°E
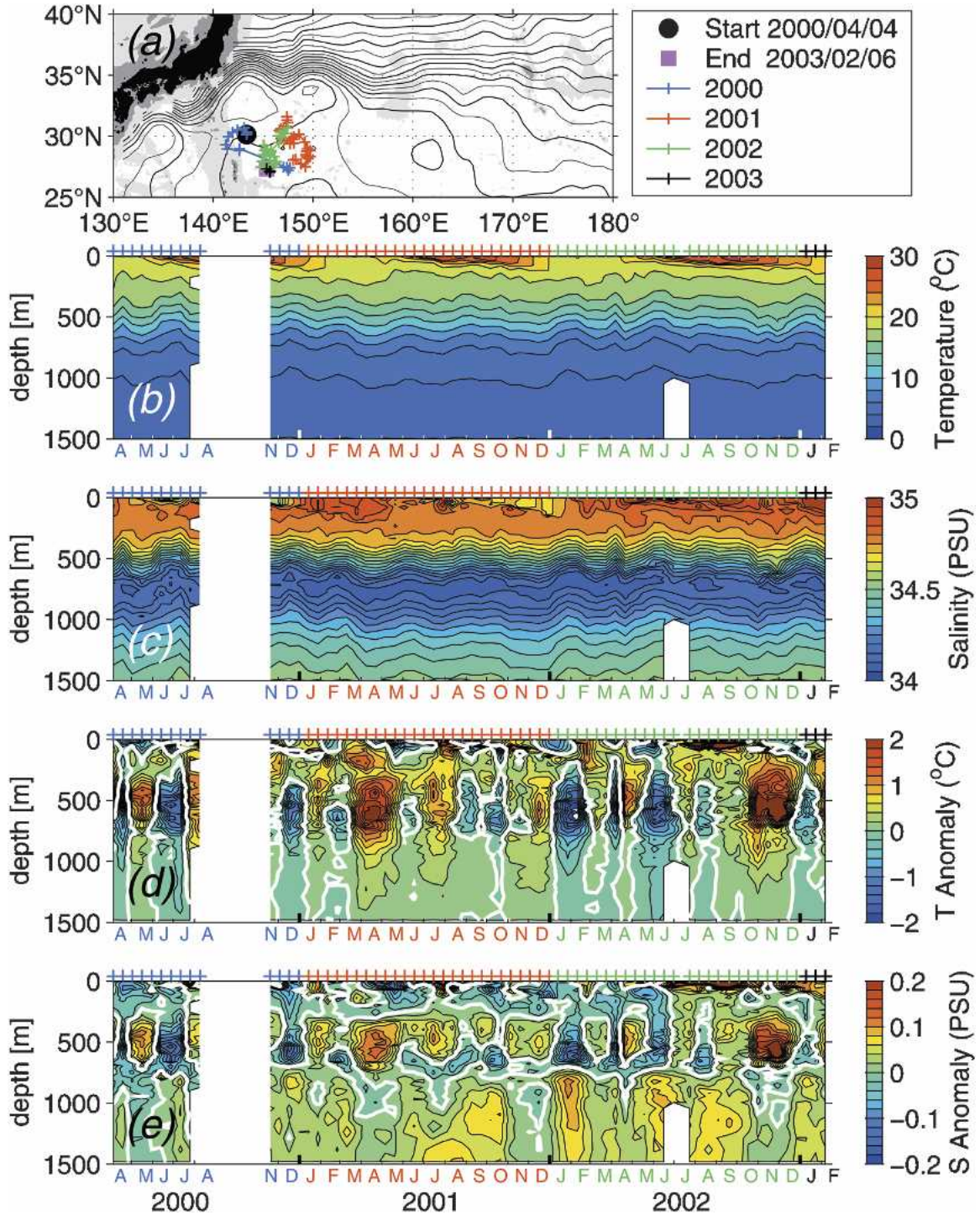
FIG. 3. (a) Trajectories of the Argo float 29033. Contours denote the mean dynamic height of the region from Teague et al. (1990). (b), (c) Temperature and salinity profiles measured by the float. (d), (e) Temperature and salinity anomaly profiles after removing the climatological T/S values of *WOA01*. Crosses denote dates of the profiling measurements.

in April 2000 as representive of the floats in the subtropical North Pacific. As shown in Fig. 3a, the float drifted in an area south of the Kuroshio Extension for a period of ~3 yr. Figure 3b shows the time series of

temperature profiles measured by the float on 10-day interval. Because of the large-amplitude seasonal surface heat flux forcing in the region, the observed upper-ocean temperatures show a well-defined annual cycle
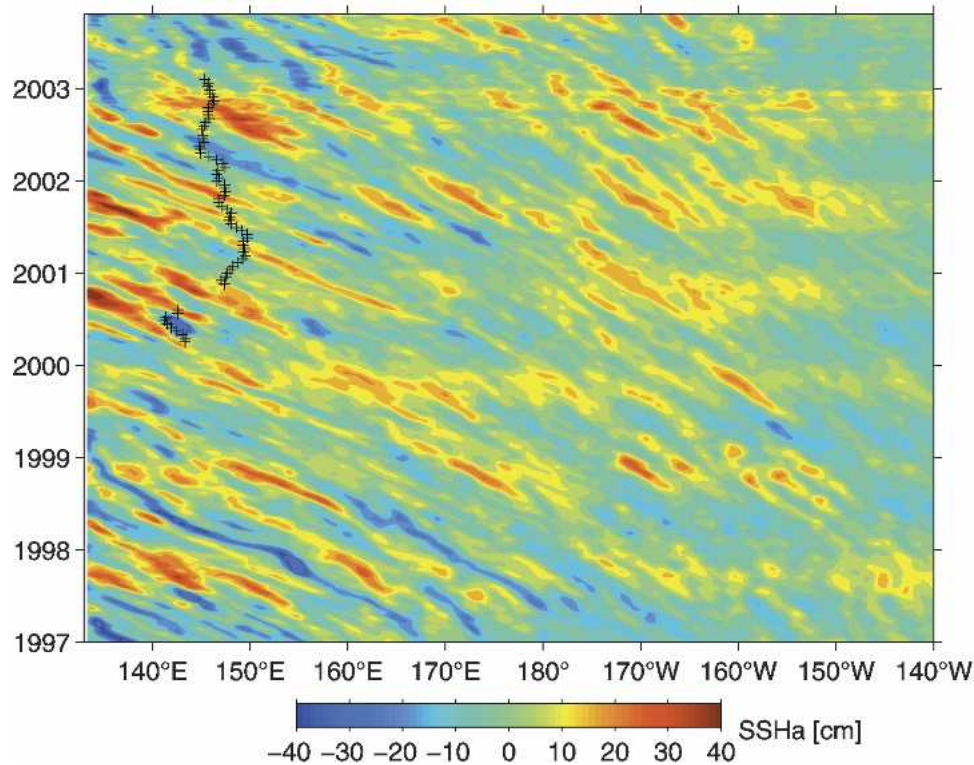
FIG. 4. Time–longitude plot of the SSH anomalies along 29°N in the North Pacific Ocean. Crosses denote the longitudinal positions and the dates for which the profiling measurements were made by the float 29033 (cf. Fig. 3).

characterized by the development of the seasonal thermocline in spring/summer and its erosion in autumn/winter. In the main thermocline below 200 m, the isotherms are observed to undulate coherently in the vertical with a typical time scale on the order of 2 months. These coherent undulations are also seen in the salinity data measured by the float (Fig. 3c).

To better describe the mesoscale perturbations captured by the float, we plot in Figs. 3d and 3e the *anomalous T–S* time series by removing climatological *T–S* profiles from the observed ones. Here, the climatological *T–S* profiles are obtained by interpolating the monthly temperature and salinity data of *WOA01* (Conkright et al. 2002) to the float's positions and times of the year. Reflecting the vertical displacement of the main thermocline, Figs. 3d and 3e show that warm (cold) anomalies are accompanied by high (low)-salinity anomalies. As the float is nearly stationary in space, the results of Fig. 3 can be regarded as a "moored" time series capturing the procession of westward-propagating warm- and cold-core eddies. Indeed, a look at the SSH anomaly data along the mean latitude of the float trajectories (29°N) reveals that the area around 145°E is populated with mesoscale eddies arriving from the east (Fig. 4). These eddies have a characteristic time scale of ~2 months and propagate westward at a speed of ~5 cm s^{-1}. It is worth emphasizing

that a very favorable agreement exists between the SSH signals measured by the satellite altimeters and those calculated dynamically from the float *T–S* data (see Fig. 5a). The complementary nature of these two measurements, with the float capturing the vertical structures of the eddies and the satellite altimetry providing detailed time-varying SSH signals, will be exploited in the following analysis.

Another notable feature revealed in Fig. 3d is that the temperature anomalies in the surface layer tend to precede those in the main thermocline. As shown in Fig. 5b, this vertical phase difference becomes more evident if we compare the time series of the temperature anomalies near the surface (at 5 m) with those near the center of the main thermocline (at 600 m). The phase shift of temperature with depth, as we noted above, is crucial for determining the heat transport carried by the eddies. The phase shift shown in Fig. 3d, however, cannot be used *directly* for heat flux calculation because both the profiling float and the mesoscale eddies are temporally drifting in space: in other words, we cannot simply convert the time coordinate in Fig. 3d to a spatial coordinate. On the other hand, as the satellite altimetric measurements provide the full time-varying SSH field, it is possible to identify the locations of the float relative to the mesoscale eddies. For example, Fig. 6 shows the sequence of the SSH anomaly
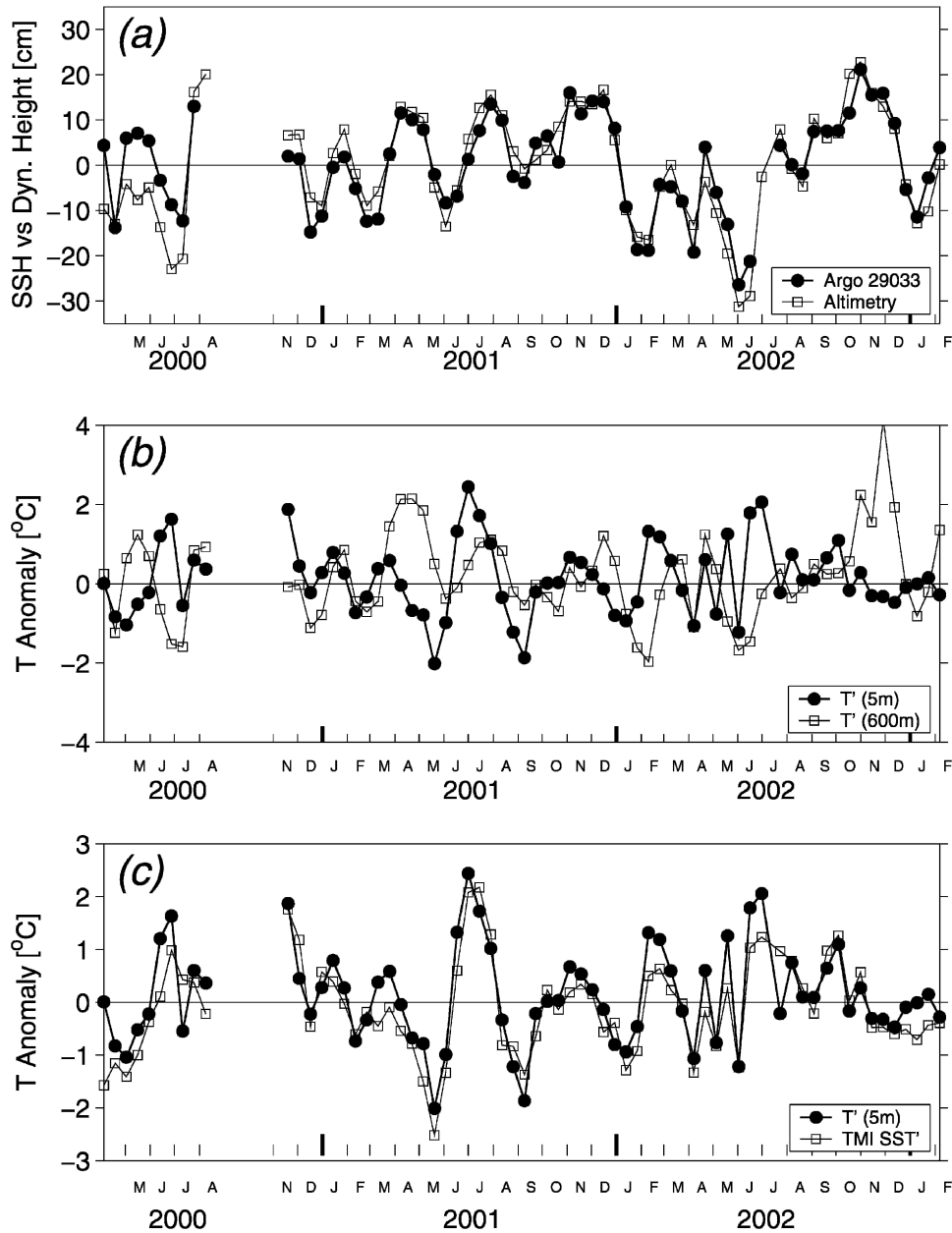
FIG. 5. (a) Time series of the surface dynamic height anomalies (0/1500 dbar) calculated dynamically from the float *T–S* data vs the SSH anomalies measured by satellite altimeters. (b) Time series of the temperature anomalies measured by the float at the 5-m depth vs those at the 600-m depth. (c) Time series of the temperature anomalies measured by the float at the 5-m depth vs the SST anomalies based on the TMI dataset.

field from 11 March to 20 May 2001, during which a westward-translating warm-core eddy passed by the profiling float (identified in the figure by the black dots). Using the information of Fig. 6, we can plot the float-derived anomalous *T–S* profiles in a reference frame moving with the eddy. As shown in Fig. 7a (left panel), this warm-core eddy has a diameter of ~300 km and a maximum temperature anomaly of 2.2°C at the core of the main thermocline. In the surface seasonal

thermocline, the warm anomaly has a magnitude of ~1.2°C and it is, as we emphasized earlier, located to the *west* of the eddy center.

The fact that the warm anomaly resides to the west of the warm-core eddy can also be discerned in Fig. 6, where warm SST anomalies (in color) appear persistently to the west of the high SSH anomalies (in contour) associated with the warm-core ring. Notice that the SST data in Fig. 6 are based on the TMI measure-
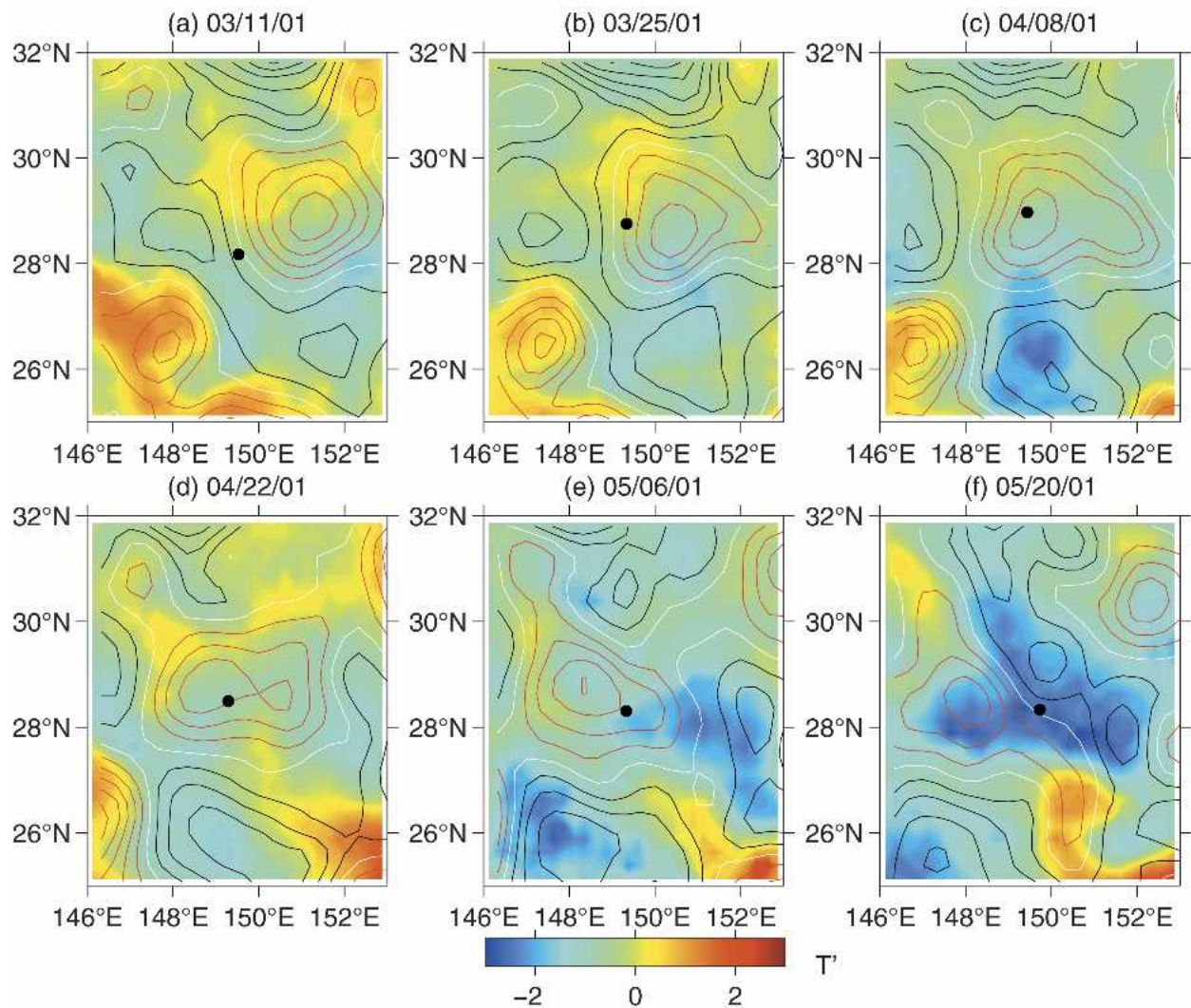
FIG. 6. Sequence of the SSH (in contour) and SST (in color) anomaly fields during 11 Mar–20 May 2001. Black dots denote the location of the Argo float 29033. Contour intervals for the SSH anomalies are 5 cm, and red, white, and black contours denote positive, zero, and negative values, respectively. The SST anomalies in each instance are formed by removing the climatological SST values of *WOA01*.

ments and they compare well to the near-surface temperature data measured by the Argo float (see Fig. 5c).

Given the anomalous temperature and salinity (not shown) profiles, we can readily calculate the geostrophic velocity of the eddy using the thermal wind equation[1] (see Fig. 7a, middle panel). By combining the anomalous temperature and velocity data, we plot in the right panel of Fig. 7a the eddy heat flux, $\rho C_p v' T'$, integrated across the eddy as a function of depth. Following Roemmich and Gilson (2001), zonal integration

limits are constrained (i.e., the edges of the eddy are chosen) such that the integrated mass transport across the eddy is zero. In the seasonal thermocline above 350 m, the heat transport is positive (northward) as a consequence of the warm anomaly being located to the west of the eddy center. Within the main thermocline the heat transport is, in general, much smaller and there is a sign change in transport between the upper and lower main thermocline. The weak transport in the main thermocline is due to the fact that the temperature anomalies there are nearly symmetric around the eddy center. The total heat transport induced by this warm-core eddy is 0.025 PW, and 87% of this amount is carried in the surface 200-m layer.

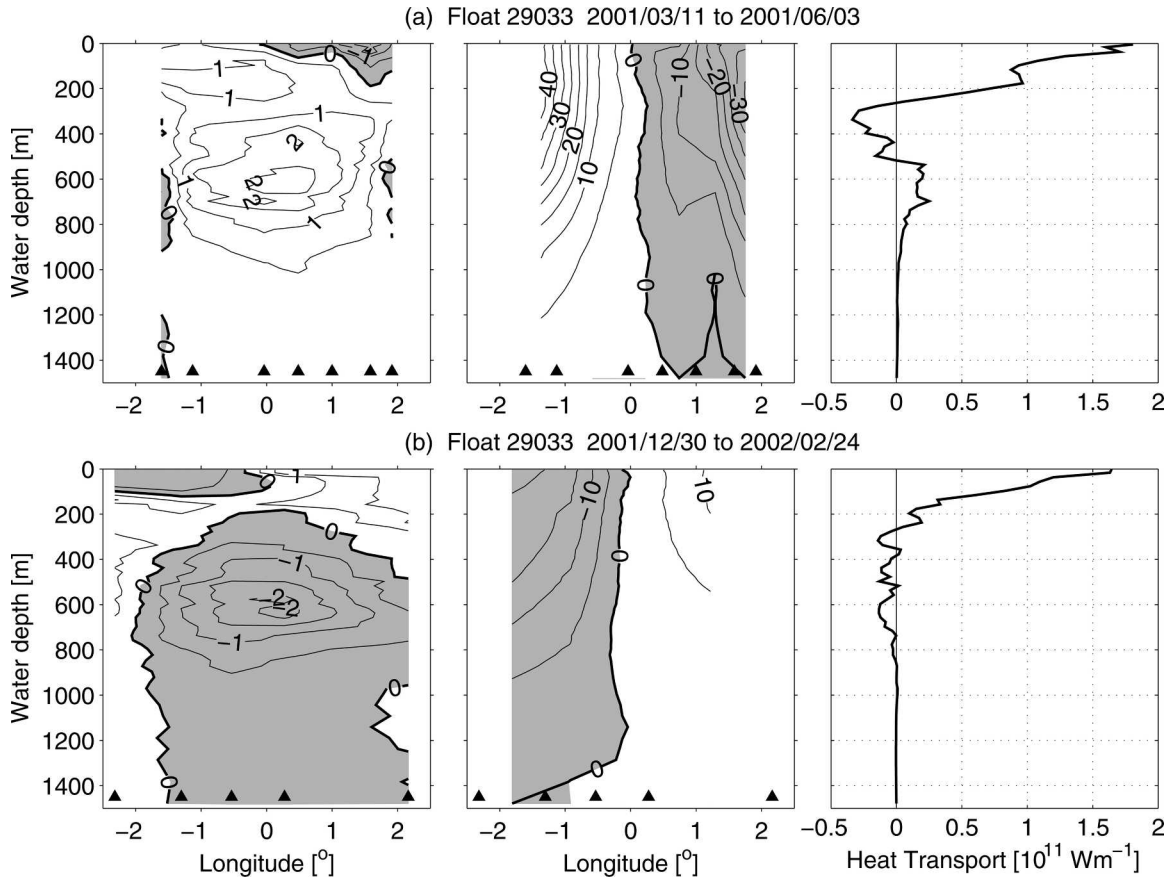To show the representativeness of this heat transport

---

[1] In this study, geostrophic velocities are calculated relative to the 1500-dbar reference level. In regions where barotropic variability is large (e.g., the Kuroshio Extension), the calculated velocities could potentially underestimate the flow field.

FIG. 7. (left) Temperature anomaly profiles (°C) plotted in the moving frame of (a) a warm-core eddy detected in 11 Mar–3 Jun 2001 and (b) a cold-core eddy detected on 30 Dec 2001–24 Feb 2002. Triangles denote the available profiles and negative anomalies are shaded. (middle) Meridional geostrophic flows associated with the warm- and cold-core eddies (cm s^{-1}; shaded areas denote southward flow). (right) Meridional heat transport $\rho c_p v' T'$ integrated across the eddy.

profile, we show in Fig. 7b the result for a cold-core eddy captured by the same Argo float during the period 30 December 2001–24 February 2002. Similar to the warm-core eddy described above, the cold temperature anomaly in the surface seasonal thermocline resides to the west of the eddy's center, and the cold temperature anomalies in the main thermocline have little vertical phase tilt. The total meridional heat transport by this cold-core eddy is 0.012 PW and most of this transport is again carried in the surface 200-m layer.

It is interesting to compare the results of Fig. 7 to the mesoscale eddies observed by Roemmich and Gilson (2001) along the San Francisco–Honolulu–Guam–Taiwan transect. By analyzing the multiyear high-resolution XBT/XCTD data, Roemmich and Gilson found that the heat transport induced by the mesoscale eddies along this transect has a vertical profile (see their Fig. 9) very similar to those presented in Fig. 7. Specifically, the poleward heat transport is mostly confined to the surface 200-m layer and a weak southward heat transport exists in the subsurface 300–400-m layer. By compositing warm- and cold-core eddies, Roem-

mich and Gilson found that a mesoscale eddy in the region typically transports 0.0054 PW northward. This value of heat transport is smaller than those found in Fig. 7 and this is likely due to the fact that the eddies generated south of the Kuroshio Extension are much stronger than those originating in the North Pacific Subtropical Countercurrent.

b. The tropical gyre

Enclosed by the zero contours of the Sverdrup transport, the tropical gyre in the North Pacific occupies the region between ~5° and ~15°N (see, e.g., Fig. 1 of Qiu and Joyce 1992). In this region the main thermocline is, in general, shallower than 400 m and typical *T–S* profiles captured by an Argo float (WMO ID: 5900270) are shown in Figs. 8b and 8c. In comparison with the temperature profiles in the subtropical gyre (Fig. 3b), seasonal near-surface temperature modulations in Fig. 8b are much weaker, indicating the lack of a regional seasonal thermocline. Figures 8d and 8e show the anomalous *T–S* profiles after removing the climatological *T–S* values. The tendency for temperature anoma-
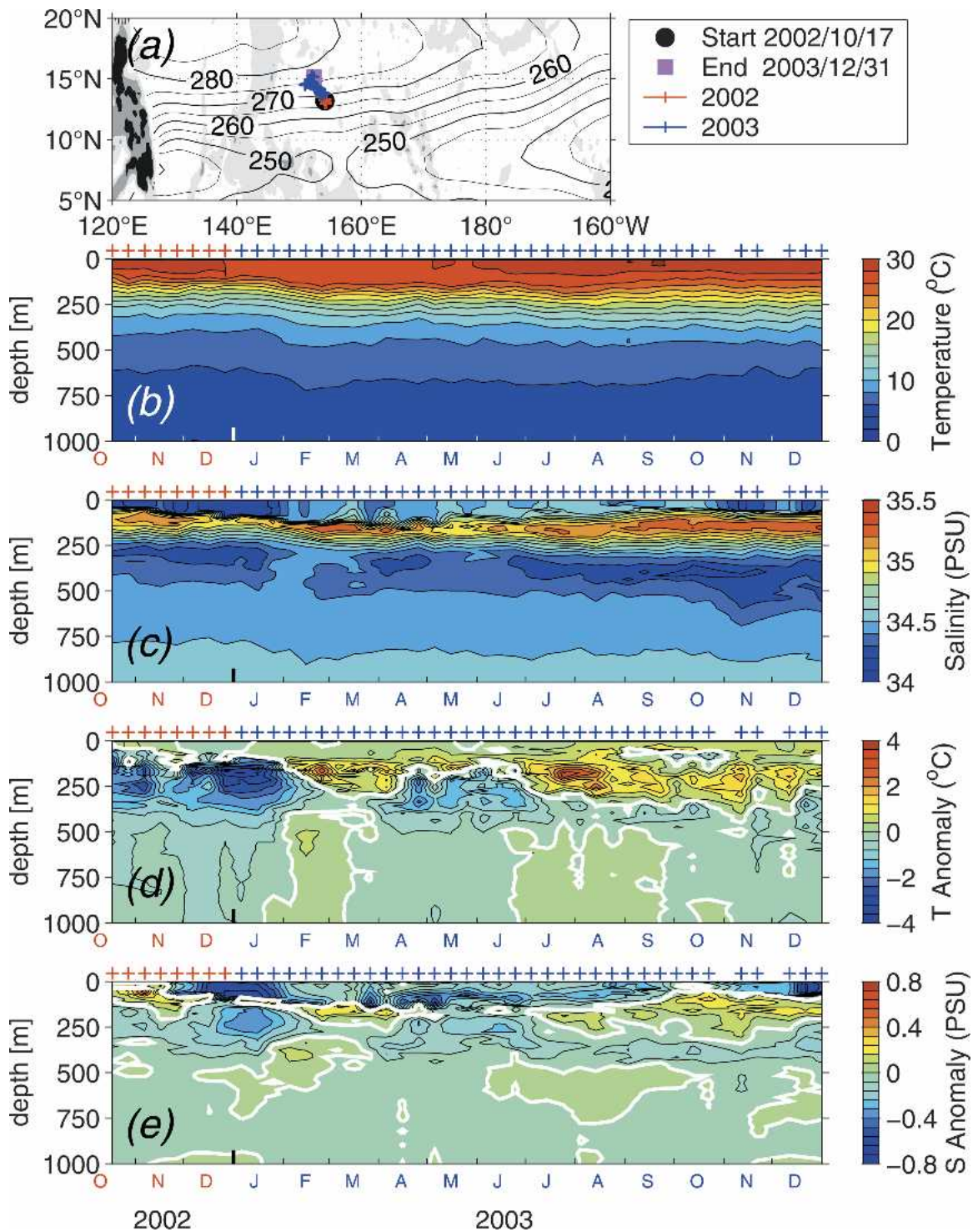
FIG. 8. As in Fig. 3, but for the Argo float 5900270 in the tropical North Pacific.

lies of the warm- and cold-core eddies to tilt *westward* with decreasing depth is again apparent in Fig. 8d. Notice that the tilt of the temperature anomalies in Fig. 8d exists throughout the main thermocline layer; this is in contrast to the subtropical eddies where the tilt of the temperature anomalies is largely confined to the near-surface seasonal thermocline (cf. Fig. 3d).

Using SSH maps similar to those presented in Fig. 6, we are able to determine again the position of the Argo float with respect to the westward-propagating meso-

scale eddies. Figure 9 (left panel) shows the vertical temperature structure of a warm-core eddy captured by the float during 4–5 February April 2003. As we noted above, the tilt of the temperature anomalies can be seen to exist in most of the upper 400-m layer. As a result of this coherent "deep" tilt, the eddy-induced heat transport is positive in the upper half of the main thermocline and negative in the lower half of the main thermocline (see the right panel of Fig. 9). With the opposing signs, the depth integrated heat transport for this warm-core eddy is only 0.0017 PW, which is an order of magnitude smaller than the heat transport values estimated for the subtropical eddies.

While the eddy-induced heat transport in the subtropical gyre has strong surface expressions, Fig. 9 reveals that the eddy-induced heat transport signal in the tropical gyre is only weakly reflected in the surface measurements. To confirm this difference between the tropical and subtropical eddies, we plot in Fig. 10 the longitudinally lagged correlation between the SST and SSH anomalies as a function of latitude in the western North Pacific Ocean (130°E–170°W). Here, the correlation is calculated based on the 6-yr (December 1997–October 2003) TMI SST and altimetric SSH data, and a high-pass filter with a zonal cutoff scale of 10° longitude has been applied to both the SST and SSH anomaly data in order to highlight the mesoscale eddy signals. In the subtropical gyre north of 15°N, Fig. 10 shows that the SST and SSH anomalies are best correlated at a lag of ∼ −0.5° longitude. Here a negative lag denotes warm (cold) SST anomalies being located to the west of high (low) SSH anomalies. This phase relationship from the satellite SST and SSH data is consistent with the finding of Fig. 7 based on the in situ Argo measurements.

In contrast to the subtropical gyre, Fig. 10 shows that the correlation between the SST and SSH anomalies is much weaker south of 15°N. This weak correlation agrees with the Argo result that the eddy-induced heat
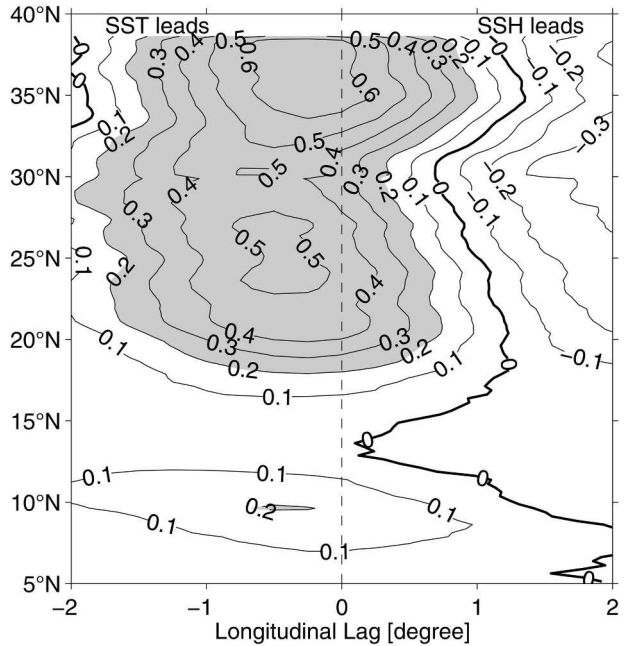

FIG. 10. Longitudinal lag correlation between the SSH and SST anomalies in the western North Pacific (130°E–170°W). To emphasize mesoscale features, both the SSH and SST anomaly data have been longitudinally high-pass filtered with a zonal cutoff scale of 10°. A negative (positive) lag here indicates a warm SST anomaly being located to the west (east) of a high SSH anomaly. Shaded areas denote where the correlation coefficient is above 0.2; assuming the degree of freedom at 120, this coefficient gives the 99% confidence level.

transport only has a weak surface expression in the tropical gyre (Fig. 9, right panel).

4. Eddy heat transport in the subtropical North Pacific

Analyses of the previous section reveal that the eddy-induced heat transport in the subtropical North Pacific
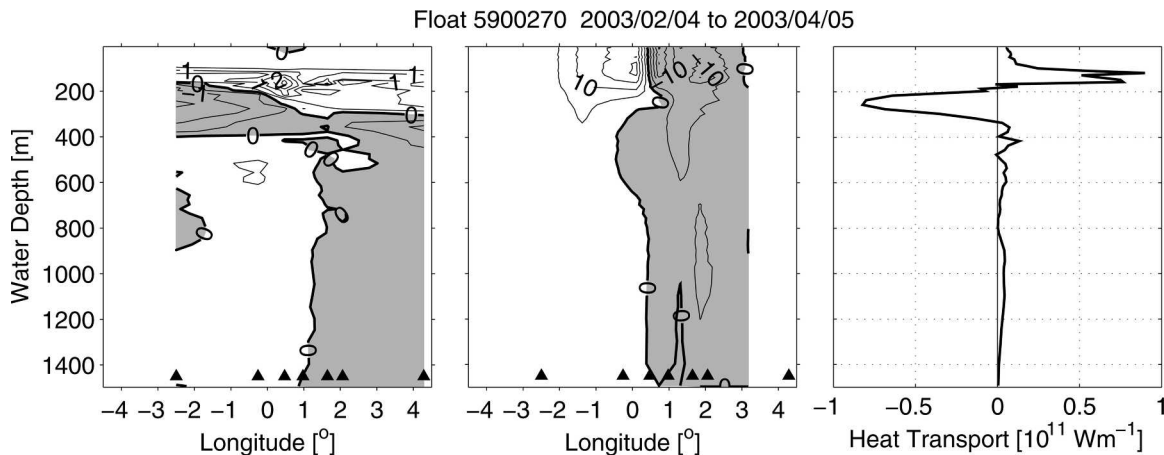

FIG. 9. As in Fig. 7, but for a warm-core ring detected on 4 Feb–5 Apr 2003 in the tropical North Pacific.

is largely confined to the seasonal thermocline of the upper ocean. This finding implies that the satellite measurements of SSH and SST, which have a much greater spatial and temporal coverage than do the subsurface *T–S* measurements, can potentially be utilized to estimate the eddy-induced heat transport on various time and length scales.

To estimate the depth-integrated heat transport from the satellite SSH and SST data, a relationship is needed that will connect the surface and depth-integrated heat transport signals. In this study, we assume this relationship to be linear; in other words, we assume there exists an effective depth H_e with which we can convert a surface eddy heat transport value to a depth-integrated value. To derive this H_e value, we use available Argo profiling data in the following way. For each consecutive pair of Argo *T–S* profiles (separated nominally by 10 days), we first remove the climatological *T–S* profiles based on the *WOA01* dataset (Conkright et al. 2002). From the paired anomalous *T–S* profiles, we calculate the meridional geostrophic velocity v' relative to the 1500-dbar reference level. If the v' value averaged in the surface 500-m layer exceeds 0.1 m s^{-1}, we regard this pair of the Argo profiles as being within a mesoscale eddy, and an effective depth H_e is calculated as

$$H_e = \int_{1,500\text{dbar}}^{0} v'T'(z)\,dz/v'T'(z=0). \quad (1)$$

For each Argo float, a mean effective depth H_e is then derived by averaging the H_e values from the available profiling pairs. (Floats with durations shorter than 100 days are excluded from this calculation.)

In Fig. 11a, we plot the H_e values estimated from the 102 Argo floats available in the North Pacific subtropical gyre as a function of the central latitude of the float's trajectories. The overall mean H_e value from the 102 floats is $\overline{H}_e = 177$ m (see the gray line in Fig. 11a). While the H_e values from the individual floats are somewhat scattered (the standard error for the estimated $\overline{H}_e$ is 16 m), there appear no noticeable latitudinal biases around the $\overline{H}_e$ value. Indeed, plotting the H_e values in a histogram reveals that its shape is close to a normal distribution (Fig. 11b), suggesting the estimated $\overline{H}_e$ is likely an unbiased mean H_e value. In the following, we will adopt $\overline{H}_e = 177$ m as the effective depth, while recognizing that there exists an uncertainty in the magnitude of this conversion value.

Figure 12 shows the estimated meridional eddy heat transport $\langle \rho c_p T'v'\overline{H}_e \rangle$ in the subtropical North Pacific based on the concurrent SST and SSH measurements of the past six years (December 1997–October 2003). Here, v' is calculated geostrophically from the SSH anomaly data, T' is from the zonally high-pass filtered TMI SST data, and angle brackets denote the temporal average. As in Fig. 10, the high-pass filter has a zonal cutoff scale of 10° longitude. Large poleward eddy heat transports can be seen in the Kuroshio Extension re-
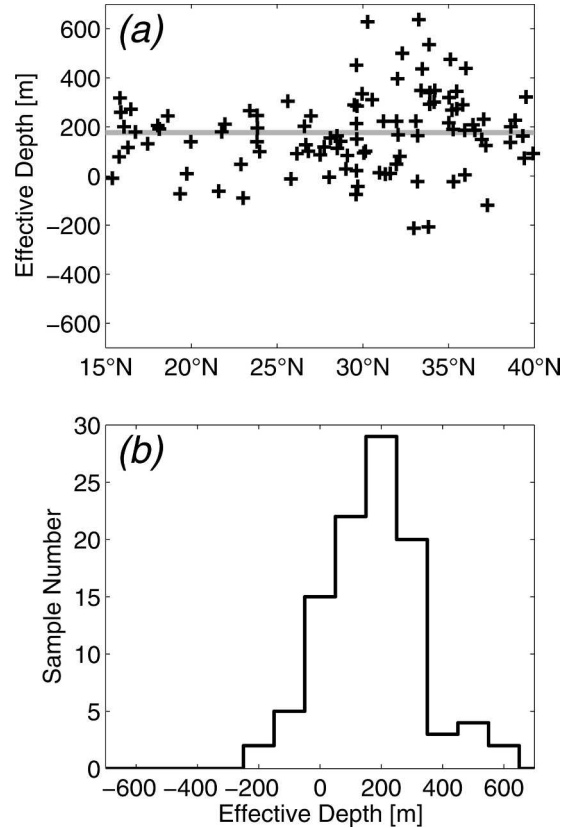

FIG. 11. (a) Effective depth (H_e) values estimated from the 102 Argo floats in the subtropical North Pacific and plotted as a function of the central latitude of each float's trajectories. The overall mean value, $\overline{H}_e = 177$ m, is indicated by the gray line. (b) Histogram of the H_e values.

gion east of Japan and in a band extending northeastward from Taiwan to the Midway Islands (around 30°N, 179°W). A third, but less strong, poleward eddy heat transport area can be seen offshore of Mexico.

Instead of a broad northward transport as shown in Fig. 1, Fig. 12 reveals that the meridional heat transport in the Kuroshio Extension region varies in direction along the path of the Kuroshio Extension jet. This reversal in direction of the meridional heat transport was also found by Wunsch (1999) based on historical moored current meter measurements in the Kuroshio Extension region. As presented in his Plates 5 and 6, the meridional eddy heat flux was estimated by Wunsch (1999) to be positive near 142°E and negative near 150°E, in good agreement with the findings of this study. Plotting the eddy heat transport values on the climatological SSH map of the region indicates that the southward eddy heat transports occur preferentially on the downstream side of the Kuroshio Extension jet's quasi-stationary meanders (Fig. 13). Note that part of this spatially alternating eddy heat transport is induced by meandering of the Kuroshio Extension jet and, when integrated spatially, it makes no net contribution
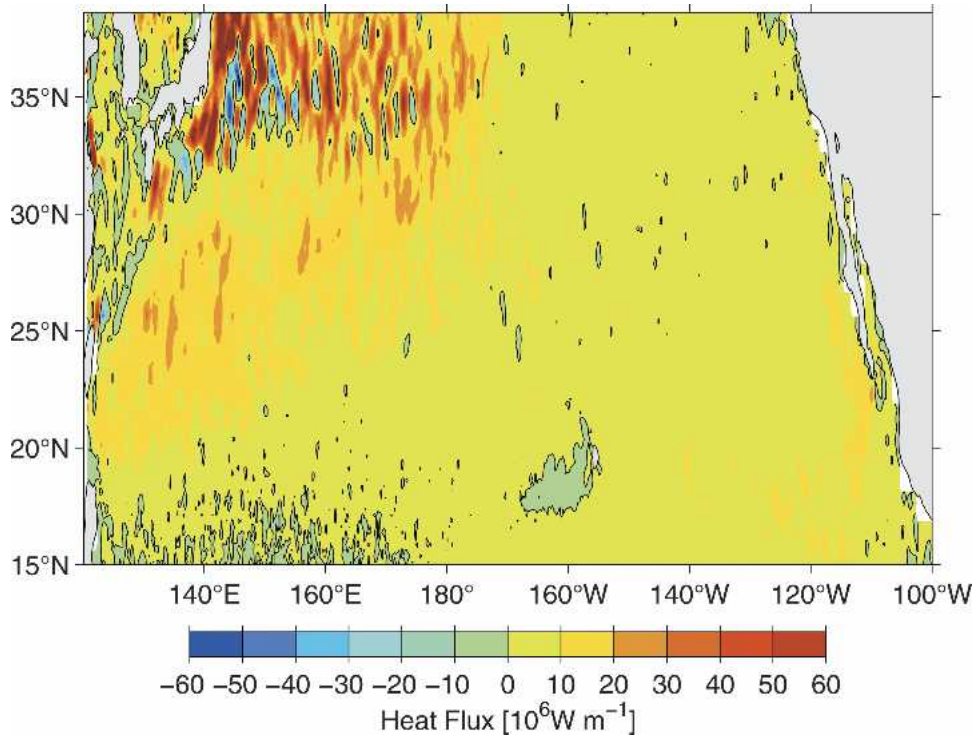
FIG. 12. Meridional eddy heat flux transport $\langle \rho c_p T' v' \overline{H}_e \rangle$ in the subtropical North Pacific. Here $T'v'$ is evaluated from the 6-yr concurrent altimetric SSH and TMI SST data, and $\overline{H}_e$ (=177 m) is based on the analysis of Argo profiling data.

to the meridional eddy heat transport across the Kuroshio Extension.

It is interesting to compare the meridional eddy heat transport estimated in Fig. 12 with that of SUW. As we noted in the introduction, SUW estimated the meridional eddy heat transport (Fig. 1) as a form of Fickian diffusion, $v'T' = -\kappa \partial \overline{T}/\partial y$, where κ was assumed to be proportional to the T/P-derived eddy kinetic energy value. Figure 14 compares the meridional eddy heat transports integrated zonally across the Pacific basin from the two studies. North of 30°N both studies show a large poleward eddy heat transport associated with the energetic Kuroshio Extension jet. The magnitude of transport from this study is smaller than from SUW and this could be due to the fact that while a meandering Kuroshio Extension jet can increase the eddy kinetic energy level effectively, it introduces *oppositely* directing eddy heat fluxes and does not necessarily lead to a large *net* meridional eddy heat transport.

In the latitudinal band of 20°–30°N, the difference between the two estimates is more substantial (see Fig. 14). In contrast to a weak poleward transport predicted by SUW, the present study suggests a sizable poleward eddy heat transport of ~0.1 PW. This eddy heat transport value may be compared with the *total* meridional heat transport across 24°N, which has been estimated to be in the range of 0.45–0.81 PW (e.g., Roemmich and McCallister 1989; Bryden et al. 1991; Macdonald 1998;

Talley 2003). As we have seen in Fig. 12, the large eddy heat transport in this band is associated with the elevated, positive eddy heat transports that extend northeastward from Taiwan to the Midway Islands. Geographically, this southwest–northeast tilting band corresponds to the location of the subtropical front (e.g., Roden 1975; White et al. 1978) where the meridional SST gradient has a regional spring and summer maximum (see Fig. 15). Accompanying this large meridional temperature gradient, the zonal current system in the region is strongly sheared in the vertical, and the occurrence of baroclinic instability (see Qiu 1999) ultimately leads to the elevated poleward eddy heat transport seen in this latitudinal band.

The difference between the present study and SUW is also substantial in the zonal band of 15°–20°N. Instead of a ~0.05-PW poleward eddy heat transport found in this study, SUW predicted a weak eddy heat transport directed *equatorward* (Fig. 14). To verify the poleward transport found in this study, we plot in Fig. 16 the meridional eddy heat transport values integrated along the repeat XBT/XCTD transect of San Francisco–Honolulu–Guam–Taiwan. The thick line shows the result based on Fig. 12 and the thin line is the result calculated by Roemmich and Gilson (2001, their Fig. 9) based on decade-long XBT/XCTD measurements. While the integrated eddy heat transport profile from the present study is spatially too smooth in comparison
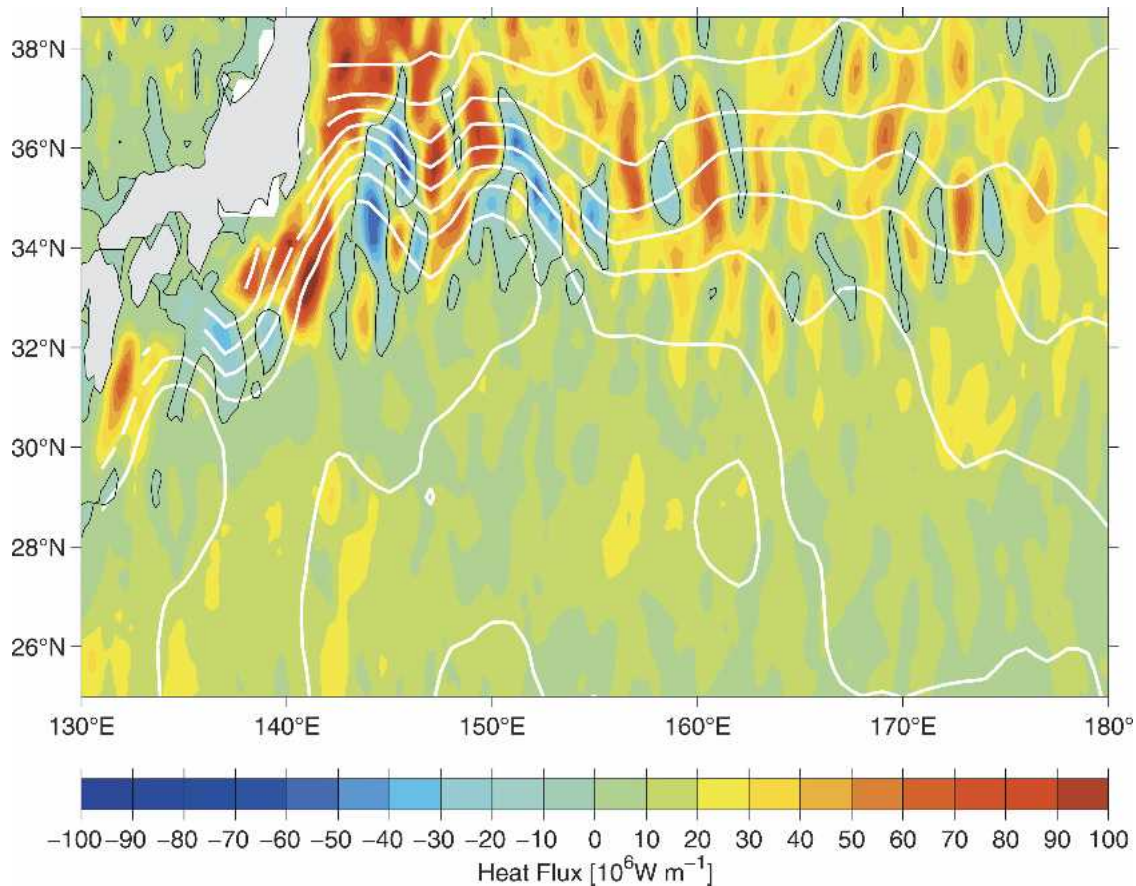
FIG. 13. As in Fig. 12 but for detailed distribution of the meridional eddy heat flux transport in the Kuroshio Extension region. White contours denote the mean surface dynamic height from Teague et al. (1990). Contour intervals are 10 cm.

with the observations (which could be caused by the oversmoothing of the CLS SSH anomaly field; see Niiler et al. 2003), it does give reasonable integrated eddy heat transport values in different sections of the
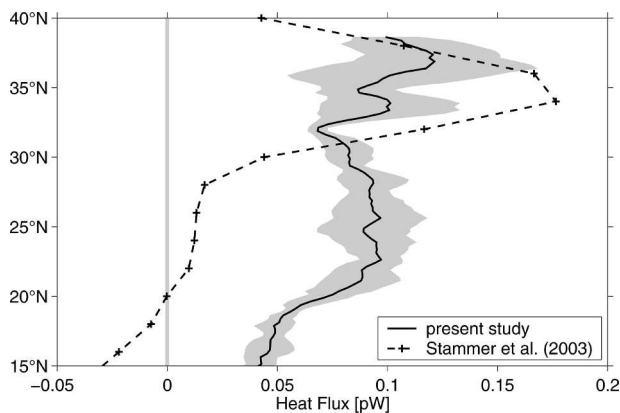

FIG. 14. Zonally integrated eddy heat transports in the subtropical North Pacific basin. Dashed line denotes the estimate based on Fig. 1 from SUW and solid line denotes the estimate based on Fig. 12. Shaded areas denote the standard deviation associated with the solid line.

transect. For example, both studies show that the poleward heat transport between San Francisco and Hawaii is ~0.01 PW, and that between Hawaii and Guam is ~0.02 PW. In the Guam–Taiwan section, the observations indicate that a significant part of the eddy heat transport (~0.03 PW) is induced by the fluctuating Kuroshio within the western boundary east of Taiwan.[2] This part, unfortunately, is not resolved by the satellite SSH and SST measurements. Outside of the western boundary, however, the present study's estimate matches again reasonably well with the in situ measurements, giving a total eddy heat transport across the XBT/XCTD transect from San Francisco to offshore of Kuroshio at 0.043 PW (see Fig. 16). Notice that integrating the meridional heat transport along the same transect using the eddy heat flux values inferred by SUW (see Fig. 1) leads to a total heat transport of −0.006 PW (not shown). The favorable comparison with the in situ measurements shown in Fig. 16 is en-

---

[2] The XBT/XCTD measurements are designed to capture the detailed structure of the Kuroshio with a spatial resolution of 10 km east of Taiwan.

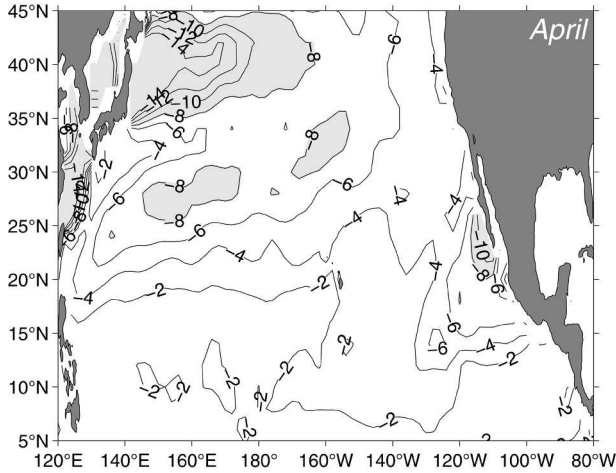FIG. 15. Meridional sea surface temperature gradient in Apr based on *WOA01* (Conkright et al. 2002) (10^{-6} °C m^{-1}). Shaded areas denote where magnitude of the SST gradient exceeds 8×10^{-6} °C m^{-1}.

couraging, as it lends support to the validity of the method adopted in this study.

Last, we note that the difference between the present study and SUW in the subtropical gyre interior can be reconciled to a certain degree if we modify the procedure of Stammer (1998) slightly. As the horizontal diffusivity κ from the mixing hypothesis is positive definite, the sign of the meridional heat transport $v'T'$ is solely determined by $-\partial \overline{T}/\partial y$. In Stammer (1998), $\overline{T}$ is defined as the mean temperature averaged in the upper 1000-m water column (see Fig. 17a). On the other hand, our analyses show that, while the eddy signals may ex-

FIG. 17. Meridional temperature gradient $\partial \overline{T}/\partial y$ from the annual mean climatology of *WOA01*, where $\overline{T}$ is averaged over the layers (a) 0–1000 m and (b) 0–200 m. Contour unit is 10^{-6} °C m^{-1}.

tend deep into the main thermocline, much of the temperature tilt, and hence bulk of the eddy heat transport, is confined to the surface 200-m layer. This result hints that a more relevant $\overline{T}$ field should be that averaged in the surface 200-m layer. As presented in Fig. 17b, the $-\partial \overline{T}/\partial y$ field in the upper 200-m layer is quite different from that of the upper 1000-m layer. This is particularly true in the 20°–30°N band, where Fig. 17b shows a localized maximum of $-\partial \overline{T}/\partial y$ associated with the Subtropical Front. Integrating $-\kappa \partial \overline{T}/\partial y$ across the Pacific basin with the temperature gradient field shown in Fig. 17b (instead of Fig. 17a) reduces the difference between the present study and SUW in the 18°–30°N band (see Fig. 18). This comparison indicates that the surface 200-m temperature field may be more relevant than the upper 1000-m temperature field for estimating the eddy heat transport based on turbulent closure schemes.

5. Summary

A method of estimating the basin-scale eddy heat transport is proposed in this study by combining satellite measurements of sea surface height and temperature and in situ profiling float data. While satellite altimetry data has been used in the past to evaluate the eddy heat transport (e.g., Stammer 1998; Holloway 1986), our method differs from these previous studies
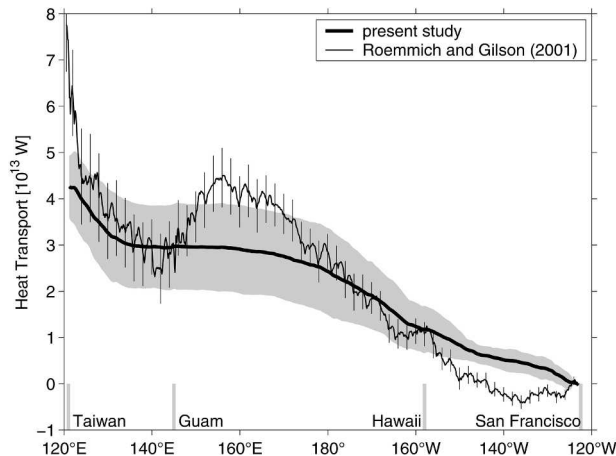

FIG. 16. Meridional eddy heat transport integrated along the XBT/XCTD transect from San Francisco to Honolulu to Guam to Taiwan. The thin line indicates the transport values calculated by Roemmich and Gilson (2001) based on high-resolution XBT/XCTD measurements, and the thick line indicates those derived from Fig. 12. Standard deviations are denoted by vertical bars and shading for the two estimates, respectively.
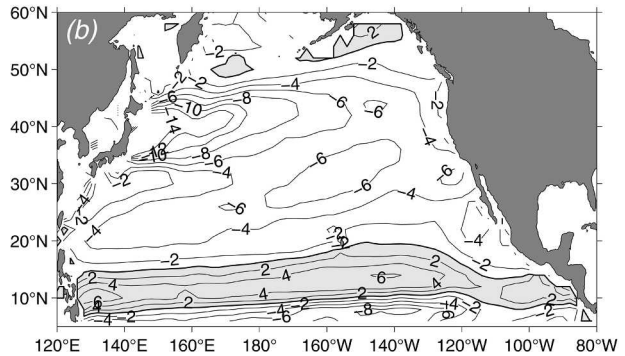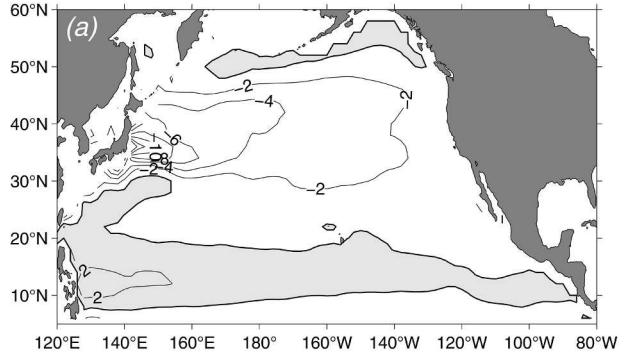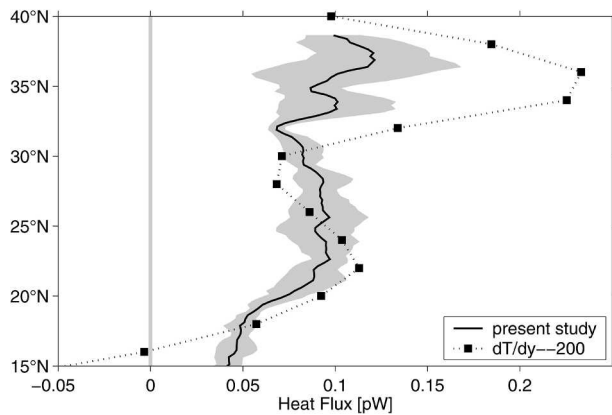
FIG. 18. As in Fig. 14 except for the dashed line, which is estimated using $-\kappa \partial \overline{T}/\partial y$, with $\partial \overline{T}/\partial y$ based on the *WOA01* temperature field averaged in the surface 200-m layer (see Fig. 17b).

by calculating the covariance of surface velocity and temperature anomalies directly, rather than resorting to turbulent closure schemes. In addition, the Argo profiling data were used in this study both to clarify the vertical structures of mesoscale eddies and to establish the relationship between the satellite-derived surface signals and those at depth.

In the subtropical gyre of the North Pacific, our analysis of the profiling float data revealed that while mesoscale eddies have their signals extending deep into the main thermocline, the eddy-induced heat transport is largely confined to the surface seasonal thermocline (0–200 m). Within this surface layer, warm (cold) surface temperature anomalies of the mesoscale eddies tend to tilt westward with decreasing depth, giving rise to a net poleward heat transport. Below the seasonal thermocline, on the other hand, temperature anomalies tend to be axisymmetric around the eddy center and make little contribution to the net heat transport. Similar vertical structures of the eddy heat transport have been observed by Roemmich and Gilson (2001) based on multiyear XBT/XCTD measurements along the San Francisco–Hawaii–Guam–Taiwan transect.

The different vertical phase tilts below and above the seasonal thermocline are likely attributable to the following reason. Within the seasonal thermocline, the background temperature gradient is being continuously reinforced by surface wind and heat flux forcing. Eddy advection of the mean temperature gradient (i.e., $\mathbf{v}' \cdot \nabla \overline{T}$) in this layer works to create the phase misalignment between the temperature and velocity anomaly fields. Below the seasonal thermocline, on the other hand, restoring of the background temperature gradient is much weaker, which causes temperature anomalies to become axisymmetric around an eddy center, diminishing the net eddy heat transport.

Confinement of the eddy-induced heat transport to the surface seasonal thermocline motivated us to seek an effective depth (H_e) that can relate the surface and

depth-integrated values of the eddy heat transport. Through analysis of the available profiling float data, the mean effective depth averaged in the subtropical gyre of the North Pacific is found to be 177 m. Using this $\overline{H}_e$ value and the concurrent satellite SSH and SST data of the past six years, we derived the basin-scale eddy heat transport and compared the result with existing studies.

In the midlatitude band of the Kuroshio Extension (32°–38°N), the basin-integrated poleward eddy heat transport is estimated at ~0.1 PW. This transport value is smaller than the previous estimates (e.g., SUW) based on turbulent closure schemes. A possible reason for this difference is that the meandering Kuroshio Extension jet introduces oppositely signed eddy heat fluxes, making it less effective in increasing the net poleward heat transport than the turbulent closure scheme estimates based on regional eddy kinetic energy (or the rms SSH) level. Away from the western boundary current, large poleward eddy heat transport was identified in a southwest–northeast-tilting band between Taiwan and the Midway Islands. This band corresponds to the region of the Subtropical Front and the large eddy heat transport is the consequence of baroclinic instability due to the vertical shear of the regional mean zonal flows (Qiu 1999). While this high eddy heat transport band was not evident in the previous studies based on the turbulent closure schemes, we showed that this band could be recovered in those studies if the relevant temperature field was chosen to be that averaged over the surface seasonal thermocline, instead of the 0–1000-m layer.

Although we have focused on the subtropical gyre of the North Pacific, the concept and method put forth in this study can be readily applied to the other subtropical basins of the world oceans. Because of the weak surface signals of eddy heat transport in the Tropics, our proposed method is, unfortunately, less applicable in the tropical oceans. Use of the TMI SST dataset, which is limited to the areas equatorward of 38°, has prevented us in this study from testing the method in the subpolar oceans. Following the launch of the Advanced Microwave Scanning Radiometer for the Earth Observing System (AMSR-E) in May 2002, a truly global SST dataset has become available recently. It will be interesting in the future to apply the method to the high-latitude oceans using this newly available global SST dataset.

REFERENCES

Argo Science Team, 2001: Argo: The global array of profiling floats. *Observing the Oceans in the 21st Century,* C. J. Koblinsky and N. R. Smith, Eds., GODAE Project Office, 248–258.

Bennett, A. F., and W. B. White, 1986: Eddy heat flux in the subtropical North Pacific. *J. Phys. Oceanogr.,* **16,** 728–740.

Bryden, H. L., and S. Imawaki, 2001: Ocean heat transport. *Ocean Circulation & Climate: Observing and Modelling the Global Ocean,* G. Siedler, J. Church, and J. Gould, Eds., Academic Press, 455–474.

——, D. Roemmich, and J. Church, 1991: Ocean heat transport cross 24°N in the Pacific. *Deep-Sea Res.,* **38,** 297–324.

Chelton, D. B., and Coauthors, 2001: Observations of coupling between surface wind stress and sea surface temperature in the eastern tropical Pacific. *J. Climate,* **14,** 1479–1498.

Conkright, M. E., R. A. Locarnini, H. E. Garcia, T. D. O'Brien, T. P. Boyer, C. Stephens, and J. I. Antonov, 2002: *World Ocean Atlas 2001: Objective Analyses, Data Statistics, and Figures, CD-ROM Documentation.* National Oceanographic Data Center, Silver Spring, MD, 17 pp.

Ducet, N., P.-Y. Le Traon, and G. Reverdin, 2000: Global high-resolution mapping of ocean circulation from TOPEX/Poseidon and *ERS-1* and *-2. J. Geophys. Res.,* **105,** 19 477–19 498.

Holloway, G., 1986: Estimation of oceanic eddy transports from satellite altimetry. *Nature,* **323,** 243–244.

Jayne, S. R., and J. Marotzke, 2001: The dynamics of ocean heat transport variability. *Rev. Geophys.,* **39,** 385–412.

——, and ——, 2002: The oceanic eddy heat transport. *J. Phys. Oceanogr.,* **32,** 3328–3345.

Keffer, T., and G. Holloway, 1988: Estimating Southern Ocean eddy flux of heat and salt from satellite altimetry. *Nature,* **332,** 624–626.

Le Traon, P.-Y., and G. Dibarboure, 1999: Mesoscale mapping capabilities of multiple-satellite altimeter missions. *J. Atmos. Oceanic Technol.,* **16,** 1208–1223.

Levitus, S., and T. Boyer, 1994: *Temperature.* Vol 4, *World Ocean Atlas 1994,* NOAA Atlas NESDIS 4, 117 pp.

Macdonald, A., 1998: The global ocean circulation: A hydrographic estimate and regional analysis. *Progress in Oceanography,* Vol. 41, Pergamon, 281–382.

Niiler, P. P., N. A. Maximenko, G. G. Panteleev, T. Yamagat, and D. B. Olson, 2003: Near-surface dynamical structure of the Kuroshio Extension. *J. Geophys. Res.,* **108,** 3193, doi:10.1029/2002JC001461.

Nonaka, M., and S.-P. Xie, 2003: Covariations of sea surface temperature and wind over the Kuroshio and its extension: Evidence for ocean-to-atmosphere feedback. *J. Climate,* **16,** 1404–1413.

Qiu, B., 1999: Seasonal eddy field modulation of the North Pacific Subtropical Countercurrent: TOPEX/Poseidon observations and theory. *J. Phys. Oceanogr.,* **29,** 2471–2486.

——, and T. M. Joyce, 1992: Interannual variability in the mid- and low-latitude western North Pacific. *J. Phys. Oceanogr.,* **22,** 1062–1079.

Roden, G. I., 1975: On the North Pacific temperature, salinity, sound velocity and density fronts and their relation to the wind and energy flux fields. *J. Phys. Oceanogr.,* **5,** 557–571.

Roemmich, D., and T. McCallister, 1989: Large scale circulation of the North Pacific Ocean. *Progress in Oceanography,* Vol. 22, Pergamon, 171–204.

——, and J. Gilson, 2001: Eddy transport of heat and thermocline waters in the North Pacific: A key to interannual/decadal climate variability? *J. Phys. Oceanogr.,* **31,** 675–687.

——, ——, B. Cornuelle, and R. Weller, 2001: Mean and time-varying meridional transport of heat at tropical/subtropical boundary of the North Pacific Ocean. *J. Geophys. Res.,* **106,** 8957–8970.

Stammer, D., 1998: On eddy characteristics, eddy transports, and mean flow properties. *J. Phys. Oceanogr.,* **28,** 727–739.

Talley, L. D., 2003: Shallow, intermediate, and deep overturning components of the global heat budget. *J. Phys. Oceanogr.,* **33,** 530–560.

Teague, W. J., M. J. Carron, and P. J. Hogan, 1990: A comparison between the Generalized Digital Environmental Model and Levitus climatologies. *J. Geophys. Res.,* **95,** 7167–7183.

Trenberth, K. E., and J. M. Caron, 2001: Estimates of meridional atmosphere and ocean heat transports. *J. Climate,* **14,** 3433–3443.

Wentz, F. J., C. Gentemann, D. Smith, and D. Chelton, 2000: Satellite measurements of sea surface temperature through clouds. *Science,* **288,** 847–850.

White, W., K. Hasunuma, and H. Solomon, 1978: Large scale season and secular variability of the subtropical front in the western North Pacific from 1954 to 1974. *J. Geophys. Res.,* **83,** 4531–4544.

Wong, A., G. C. Johnson, and W. B. Owens, 2003: Delayed-mode calibration of autonomous CTD profiling float salinity data by θ–S climatology. *J. Atmos. Oceanic Technol.,* **20,** 308–318.

Wunsch, C., 1999: Where do ocean eddy heat fluxes matter? *J. Geophys. Res.,* **104,** 13 235–13 249.